Special issue of International Journal of Computer Vision manuscript No.
(will be inserted by the editor)

Numerical LDDMM of m-currents with finite elements

Andreas Günther · Hans Lamecker · Martin Weiser

Received: date / Accepted: date

Abstract We present a unified computational framework for matching 3d geometric objects (points, lines, surfaces, volumes) of highly varying shape. Our approach is based on the Large Deformation Diffeomorphic Metric Mapping (LDDMM) method acting on m-currents. After stating an optimization algorithm in the function space of admissible morph generating velocity fields, two innovative aspects in this framework are presented: First, we spatially discretize the velocity field with conforming adaptive finite elements and discuss advantages of this new approach. Secondly, we directly compute the temporal evolution of discrete m-current attributes. Several numerical experiments demonstrate the effectiveness of this approach.

Keywords Large deformation · Diffeomorphic registration · Matching · Currents · Adaptive finite elements

Mathematics Subject Classification (2000) 58A25 · 37E30 · 58J72 · 49J20 · 65N30

1 Introduction

The *Large Deformation Diffeomorphic Metric Mapping* (LDDMM) approach initiated in Dupuis et al (1998) and Trouvé (1995) has attracted considerable attention over the last few years in medical imaging. It allows to match highly deformed objects and as such is capable of performing inter-individual registration. LDDMM constructs a space mapping by evolving a displacement field along a velocity field, we call *wind*. Depending on the regularity of the wind, either *diffeomorphisms* (Beg et al 2005; Marsland and Twining 2004) or *homeomorphisms* (Younes 2010) of the embedded space can be obtained. Thus, it provides a basis for many applications of anatomical shape analysis, where a one-to-one correspondence between different geometric objects is required.

The LDDMM technique is commonly applied for matching *currents* (Durrleman 2010). Currents provide a unified mathematical description of geometric objects of dimension 0 (points), 1 (curves), 2 (surfaces) or 3 (volumes) (Federer 1996; Morgan 2009).

Embedded in $\mathbb{R}^3$ m-currents form linear spaces, are equipped with an inner product and hence are a suitable tool for statistical shape analysis (Durrleman 2010). The induced norm provides a similarity measure for matching of source and target objects.

The usual wind parametrization constructs travelling radial basis functions coupled to the current discretisation. In Joshi and Miller (2000) it is proven, that for matching pairs of finitely many landmarks attaching a momentum vector at each vertex of the source shape is the wind structure for the optimal solution. However, this structure is no longer optimal for the cases of matching lines, surfaces or volumes. Therefore other approaches to describe the wind field have been considered.

In Cotter (2008) a particle-mesh method has been applied to 1-currents in 2D. Therein curves of same topology represented by a parameterization were ap-

We acknowledge support by DFG-Matheon Project F2.

A. Günther
Zuse Institute Berlin, Takustraße 7, 14195 Berlin, Germany
Tel.: +49-30-84185262
Fax: +49-30-84185107
E-mail: guenther@zib.de

H. Lamecker
Zuse Institute Berlin, Takustraße 7, 14195 Berlin, Germany

M. Weiser
Zuse Institute Berlin, Takustraße 7, 14195 Berlin, Germany

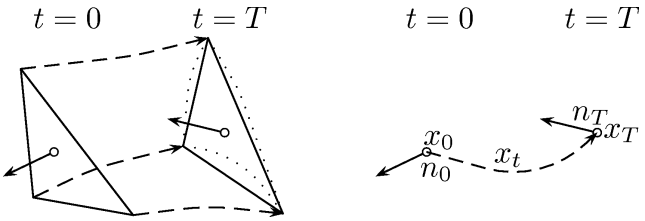

Fig. 1 Usual discrete 2-current deformation (left) versus the direct approach (right)

proximated by a finite point set without any tangential information regardless of some geometric level of detail for matching. Cotter proposes to use cubic B-splines on a fixed grid for the wind discretization and hence decouples wind- and current-discretization. In an enclosed efficiency discussion this sub-optimal parameterization is still competitive due to the simpler wind structure. However, the numerical scheme there relies on equidistant cartesian grids with constant diffusity in order to apply FFT techniques.

In contrast to Cotter (2008), we consider a 3D setting and apply the *Orthogonal Matching Pursuit* (OMP) proposed in Durrleman et al (2009) to obtain a sparse representation for general m-currents at a given geometric resolution (spectral length) in terms of a sum of discrete *Dirac delta m-currents*. Currently, the LDDMM evolution of this representation is only done indirectly via an approximative scheme (Durrleman 2010, Rem. 4.13) as depicted in Fig. 1 (left) for $m = 2$, because it would otherwise require the computation of the Jacobian of the diffeomorphism, which is a challenge when discretizing the wind using Gaussian kernels (Glaunès et al 2008, 2004; Vaillant and Glaunès 2005).

In this paper, we study the *direct* evolution of Dirac delta m-currents (right of Fig. 1). We show that the direct approach allows to uniformly treat m-currents for $m = 0, \dots, 3$ (Sec. 2), which to the best of our knowledge has not been shown before. We show also how to compute the Jacobian in this setting by using *finite elements* (FE) to discretize the wind in the LDDMM framework (Sec. 3). Since the compactly supported basis functions are fixed in space the computation is significantly simplified. In contrast to Cotter (2008), we also consider locally refined meshes and exploit the decoupling of the wind and current discretization for an adaptive current representation, giving a significant reduction of degrees of freedom (Sec. 4).

2 Continuous matching problem

For given shapes $\mathcal{S}, \mathcal{T} \subset \mathbb{R}^3$ we aim at constructing a sufficiently smooth bijection ϕ of $\mathbb{R}^3$ such that the distance between $\phi(\mathcal{S})$ and $\mathcal{T}$ is minimal. Here we give a precise formulation of the resulting optimization problem.

2.1 Currents

Currents are mathematical tools suited for describing geometric objects such as points, space curves, surfaces and volumes embedded in $\mathbb{R}^3$. Their precise definition from Federer (1996); Morgan (2009) requires notation for differential forms taken from Morita (2001). Let for $m = 0, 1, 2, 3$ the set $\mathcal{D}^m := C_c^\infty(\mathbb{R}^3, \Lambda^m\mathbb{R}^3)$ denote the vector space of all C^∞ *differential m-forms* on $\mathbb{R}^3$ with compact support. An m-current is an element of $\mathcal{D}_m$, the dual space of $\mathcal{D}^m$. The elementary *Dirac delta m-currents* $\delta_x^{u_1 \wedge \dots \wedge u_m} \in \mathcal{D}_m$ act on $\omega \in \mathcal{D}^m$ as

$$\delta_x^{u_1 \wedge \dots \wedge u_m}(\omega) = \omega(x)(u_1 \wedge \dots \wedge u_m),$$

where $\wedge$ denotes a multilinear alternating wedge product between 3-vectors. Following the discussion in (Durrleman 2010, Sect. 1.5.1) it turns out that for the purpose of matching currents the testspace of all C^∞ differential m-forms is not suited due to a missing bound in variation. Moreover the space $\mathcal{D}^0$ can be identified with scalar C_c^∞ functions on $\mathbb{R}^3$. For $m = 1$ and $m = 2$ the space $\mathcal{D}^m$ is isomorphic to the space of vector-valued C_c^∞ functions from $\mathbb{R}^3$ to $\mathbb{R}^3$. An element of $\mathcal{D}^3$ can be written as a scalar C_c^∞ function times the determinant form on $\mathbb{R}^3$.

Both aspects motivate the use of *Reproducible Kernel Hilbert Spaces* (RKHS) W^m as testspaces.

Definition 1 Let $d_m = 1$ for $m \in \{0, 3\}$ and $d_m = 3$ for $m \in \{1, 2\}$. For $m = 0, 1, 2, 3$ let W^m be the span of d_m-vectorfields still denoted by $\omega(x) = k_m(x, y)a$, where $x, y \in \mathbb{R}^3$, $a \in \mathbb{R}^{d_m}$ and $k_m(x, y) = \exp(-\|x - y\|^2/\sigma_m^2)$. The space W^m can be equipped with the inner product

$$\langle k_m(\cdot, x)a, k_m(\cdot, y)b \rangle_{W^m} = a^* k_m(x, y)b \ .$$

Here the symbol $*$ denotes the transpose operation.

An *m-current* in $\mathbb{R}^3$ is a continuous linear functional on W^m. W_m denotes the vector space of all m-currents in $\mathbb{R}^3$.

For $x \in \mathbb{R}^3$ and *attribute* $a \in \mathbb{R}^{d_m}$ we define the elementary *Dirac delta m-currents* $\delta_x^a \in W_m$ acting on $\omega \in W^m$ as $\delta_x^a(\omega) = a^*\omega(x)$.

The above inner product induces a norm on W^m, which can be computed efficiently via *Fast Gauss Transform* (FGT) even for a large number of linear combinations of the above basis functions. The chosen Gaussian kernel k_m can be considered as Green's function for some

differential operator L_W (see Beg et al (2005); Durrleman et al (2009); Glaunès et al (2008)). With the above objects at hand the Riesz representation theorem provides a unique operator $K_W^m : W_m \to W^m$ reflecting the canonical isometry between W^m and W_m defined via

$$\langle K_W^m f, g\rangle_{W^m} = \langle f, g\rangle_{W_m, W^m} = f(g)$$

for all $f \in W_m$ and $g \in W^m$. It provides for the m-current $\mathcal{S}^m$ the Riesz representant $K_W^m \mathcal{S}^m$ as unique d_m-vectorfield on $\mathbb{R}^3$.

2.2 Homeomorphisms and diffeomorphisms

Let Ω be an open bounded subset of $\mathbb{R}^3$ and consider functions $v_t : \bar{\Omega} \to \mathbb{R}^3$ that vanish on $\partial\Omega$. For given final time $T > 0$ and time-dependent wind $v = (v_t)_{t\in[0,T]}$ we consider the temporal evolution of the identity map

$$\frac{\partial \phi_t^v}{\partial t} = v_t(\phi_t^v) \text{ with } \phi_0^v(x) = x \ . \tag{1}$$

In what follows it will be useful to define the *trajectory* $x_t := \phi_t^v(x)$ for some fixed space point $x \in \mathbb{R}^3$ and the map $\phi_{st}^v := \phi_t^v \circ (\phi_s^v)^{-1}$, describing the movement of a particle starting in x at time s towards $\phi_{st}^v(x)$ at time t. It is well known (see Thm. C.3 of Younes (2010)), that (1) is uniquely solvable when for some $x_0 \in \Omega$ the integral $\int_0^T \|v_t(x_0)\|_{\mathbb{R}^3} + \mathrm{Lip}(v_t)\, dt$ is bounded. Furthermore its solution $\phi_t^v : \mathbb{R}^3 \to \mathbb{R}^3$ is a *homeomorphism* of Ω for all times $t \in [0, T]$. Under more restrictive assumptions onto the spatial smoothness of the wind, i.e.

$$v_t \in C_0^1(\Omega, \mathbb{R}^3)\ \forall t \in [0,T] \text{ and } \int_0^T \|v_t\|_{1,\infty}\, dt < \infty$$

the unique solution of (1) is even a *diffeomorphism* of Ω for all times $t \in [0, T]$ (see Thm. 8.7 of Younes (2010)). For convenience we look for the wind v_t in some Hilbert space V. Such spaces can be constructed by defining inner products associated to differential operators. Let therefore $L : V \to L^2(\mathbb{R}^3)$ be a differential operator and equip the Hilbert space V with the inner product $\langle v_t, g\rangle_V = \langle Lv_t, Lg\rangle_{L^2} = \langle L^*Lv_t, g\rangle_{V^*,V}$. Here L^* denotes the adjoint operator. For this work we use

$$S := L^*L = (-\mathrm{div}(\sigma_V^2 \nabla) + I)^k = (-\sigma_V^2 \Delta + I)^k \tag{2}$$

and $k = 1$ or $k = 2$ giving the Sobolev spaces H^k (see Glaunès et al (2008)). For given $f \in V^*$ we consider solutions $v_t \in V$ of $Sv_t = f$ with homogeneous Dirichlet boundary conditions for v_t (and v_t' if $k = 2$). Here the real parameter $\sigma_V > 0$ balances between smoothing and data fitting of the right hand side f. For other choices of L^*L and boundary conditions see Marsland and Twining (2004). Dealing with natural boundary conditions is also possible, but requires a sufficiently large domain to keep all trajectories therein. Analogous to K_W^m we introduce the isometry operator $K_V : V^* \to V$. A mathematically equivalent approach of constructing V consists in defining K_V via the Green's function $k_V(x, y)$ of L^*L, see for instance Glaunès et al (2008, 2004); Vaillant and Glaunès (2005); Vaillant et al (2004).

Table 1 Pushforwards of Dirac delta m-currents under ϕ

$m = 0$	$d_0 = 1$	$c \in \mathbb{R}$	$\phi_\sharp(\delta_x^c) = \delta_{\phi(x)}^c$
$m = 1$	$d_1 = 3$	$\tau \in \mathbb{R}^3$	$\phi_\sharp(\delta_x^\tau) = \delta_{\phi(x)}^{d_x\phi(\tau)}$
$m = 2$	$d_2 = 3$	$n \in \mathbb{R}^3$	$\phi_\sharp(\delta_x^n) = \delta_{\phi(x)}^{\lvert d_x\phi\rvert d_x\phi^{-*}(n)}$
$m = 3$	$d_3 = 1$	$\rho \in \mathbb{R}$	$\phi_\sharp(\delta_x^\rho) = \delta_{\phi(x)}^{\lvert d_x\phi\rvert\rho}$

2.3 Diffeomorphic deformation of currents

Definition 2 For $m = 0, 1, 2, 3$ let currents $\mathcal{S}^m \in \mathcal{D}_m$ be given. Let ϕ denote a diffeomorphism on $\mathbb{R}^3$ and $d_x\phi$ the Jacobian of ϕ at x. For a differential form $\omega \in \mathcal{D}^m$, $\phi^\sharp\omega \in \mathcal{D}^m$ is called the *pullback* by ϕ (see e.g. Morita (2001)) and is defined via

$$\phi^\sharp\omega(x)(u_1 \wedge \ldots \wedge u_m) = \omega(\phi(x))(d_x\phi(u_1) \wedge \ldots \wedge d_x\phi(u_m))$$

for all $x \in \mathbb{R}^3$. The *pushforward* $\phi_\sharp\mathcal{S}^m \in \mathcal{D}_m$ of $\mathcal{S}^m$ under ϕ is defined via

$$\phi_\sharp\mathcal{S}^m(\omega) = \mathcal{S}^m(\phi^\sharp\omega) \text{ for all } \omega \in \mathcal{D}^m \ .$$

If $\mathcal{S}^m$ is associated to a sub-manifold in $\mathbb{R}^3$, its pushforward $\phi_\sharp\mathcal{S}^m$ under ϕ corresponds to the *deformed* submanifold $\phi(\mathcal{S}^m)$. This important property justifies to write also $\phi(\mathcal{S}^m) \in \mathcal{D}_m$. The explicitly calculated pushforwards for elementary Dirac delta m-currents taken from Tab. 1.2 of Durrleman (2010) are given in Tab. 1.

Let some wind v be given and consider the family $(\phi_t^v)_t$ of diffeomorphisms generated via (1). The following theorem describes the direct evolution of m-current attributes $a \in \mathbb{R}^{d_m}$ under $(\phi_t^v)_t$, where $'$ denotes the time derivative.

Theorem 1 *The pushforwards of $\delta_{x_0}^{c_0}$, $\delta_{x_0}^{\tau_0}$, $\delta_{x_0}^{n_0}$ and $\delta_{x_0}^{\rho_0}$ under ϕ_s^v satisfying* (1) *are $\delta_{x_s}^{c_0}$, $\delta_{x_s}^{\tau_s}$, $\delta_{x_s}^{n_s}$ and $\delta_{x_s}^{\rho_s}$. Their components are given via the ODEs*

$$\begin{aligned}
x_t' &= v_t(x_t) && \text{with } x(0) = x_0\\
\tau_t' &= (d_{x_t}v_t)\tau_t && \text{with } \tau(0) = \tau_0\\
n_t' &= n_t\mathrm{tr}(d_{x_t}v_t) - (d_{x_t}v_t)^* n_t && \text{with } n(0) = n_0\\
\rho_t' &= \rho_t\mathrm{tr}(d_{x_t}v_t) && \text{with } \rho(0) = \rho_0 \ .
\end{aligned}$$

Proof Abbreviating $J_t = d_{x_0}\phi_t^v$ and $A_t = d_{x_t}v_t$ there holds (see Beg et al (2005)) $J_t' = A_t J_t$ with $J(0) = I_3$. Observing the evolution of the Wronskian (Mattheij and Molenaar 2002, Thm. 2.14) or via Jacobi's formula one obtains

$$|J_t|' = |J_t|\mathrm{tr}\left(J_t^{-1}J_t'\right) = |J_t|\mathrm{tr}\left(J_t^{-1}A_tJ_t\right) = |J_t|\mathrm{tr}(A_t),$$

where $\mathrm{tr}(A)$ denotes the trace of a matrix A and $A^{-*} = (A^{-1})^*$. Now from Tab. 1 we read out

$$\begin{aligned} x_t &= \phi_t^v(x_0) \\ \tau_t &= J_t\tau_0 \\ n_t &= |J_t|J_t^{-*}n_0 \\ \rho_t &= |J_t|\rho_0 \ . \end{aligned}$$

Differentiation of the above equations with respect to t yields

$$\begin{aligned} x_t' &= \phi_t^v(x_0)' = v_t(\phi_t^v(x_0)) = v_t(x_t) \\ \tau_t' &= J_t'\tau_0 = A_tJ_t\tau_0 = A_t\tau_t \\ n_t' &= |J_t|'J_t^{-*}n_0 + |J_t|(J_t^{-*})'n_0 \\ &= |J_t|\mathrm{tr}(A_t)J_t^{-*}n_0 - |J_t|A_t^*J_t^{-*}n_0 \\ &= n_t\mathrm{tr}(A_t) - A_t^*n_t \\ \rho_t' &= |J_t|'\rho_0 = |J_t|\mathrm{tr}(A_t)\rho_0 = \rho_t\mathrm{tr}(A_t), \end{aligned}$$

which proves the assertion. □

Remark 1 The authors emphasize the striking advantage that Theorem 1 enables to find the final position and attribute of a Dirac delta m-current without computing the Jacobian of the deformation. The appearing ODEs only involve the Jacobian of the velocity fields, which will be given in a closed form in any case.

Independently of the LDDMM approach but similar to the pushforward of 3-currents, Burger et al (2011) consider mass-preserving hyperelastic image registration, where the determinant of the deformations' Jacobian is explicitly monitored.

Let us visualize the actual situation of Theorem 1 in Fig. 2. A Dirac delta 0-current δ_x^c is displayed as a c-colored ball with midpoint x. The scalar c is considered as a parameter in a colormap. A Dirac delta 1-current δ_x^τ is displayed as vector τ starting from $x - \tau/2$. A Dirac delta 2-current δ_x^n is displayed as disc with midpoint x, area $|n|$ and surface normal n. The 3-current δ_x^ρ is drawn as a ball of volume ρ and midpoint x. The first row of Fig. 2 is devoted to the case $a_t' = 0$, i.e. the wind vectorfield v_t generates a local translation such that the attribute does not change. On the other hand we consider wind vectorfields v_t such that the point x remains fixed, i.e. $x_t' = 0$. Here we distinguish between the scalar valued case $m = 3$, where basically local spatial explosions (or implosions) have impact on the sphere volume ρ and the vector valued case $m = 1$ or $m = 2$, where additionally a rotational component of the wind influences vectors. In general, a superposition of all such effects may appear. It is clear, that in order to control current position x and attribute a the space of wind vectorfields needs to be sufficiently large.

2.4 Optimization problem in function space

Let source $\mathcal{S}^m \in W_m$ and target current $\mathcal{T}^m \in W_m$ be given for $m = 0, \ldots, 3$. For given wind v we define the deformed current $\mathcal{S}_t^m := \phi_t^v(\mathcal{S}^m)$ at time t. *Matching* means the minimization of the distance of the deformed source current at final time $\mathcal{S}_T^m$ to its target current $\mathcal{T}^m$, i.e. minimizing the dual norm $\|\phi_T^v(\mathcal{S}^m) - \mathcal{T}^m\|_{W_m} = \|\mathcal{S}_T^m - \mathcal{T}^m\|_{W_m}$ in the space of m-currents.

Given a regularization parameter $\gamma > 0$ and matching weights $\lambda_m \geq 0$ we consider for $v \in L^2([0,T],V)$ the following optimization problem:

$$J(v) := \gamma \int_0^T \|v_t\|_V^2 \, dt + \sum_{m=0}^{3} \lambda_m \|\phi_T^v(\mathcal{S}^m) - \mathcal{T}^m\|_{W_m}^2 \to \min \ . \quad (3)$$

Here the first summand involves the kinetic energy of the wind. The existence of a solution for (3) is proven in Glaunès (2005), however it is generally not unique (Cao et al 2005). Following Glaunès et al (2004), the gradient of J in $L^2([0,T],V)$ at fixed v is given by $(\nabla J)_t = 2\gamma v_t + 2K_V(f_t)$, where $f_t \in V^*$ is defined by

$$f_t(u) = \sum_{m=0}^{3} \lambda_m \langle \mathcal{S}_t^m, \nabla(K_W^m(\mathcal{S}_T^m - \mathcal{T}^m) \circ \phi_{tT}^v)^* u \rangle_{W_m, W^m}$$

for all $u \in V$. For further discussion concerning the choice of the gradients metric we refer the reader to Beg et al (2005). With the above quantities at hand one is able to state a steepest descent optimization algorithm in the function space of velocity fields v.

Remark 2 In order to keep the presentation as simple as possible we consider until Sec. 4 only one RKHS W^m with one spectral width $\sigma_m > 0$. However, all investigations carry over for a family of spaces $W^{m,i} = W^m(\sigma_{m,i})$ with $\sigma_{m,i} \in \Sigma_m \subset \mathbb{R}_+$. The extended optimization problem then reads:

$$\gamma \int_0^T \|v_t\|_V^2 \, dt + \sum_{m=0}^{3} \lambda_m \sum_{\sigma_{m,i} \in \Sigma_m} \|\phi_T^v(\mathcal{S}^m) - \mathcal{T}^m\|_{W_{m,i}}^2 \to \min \ . \quad (4)$$

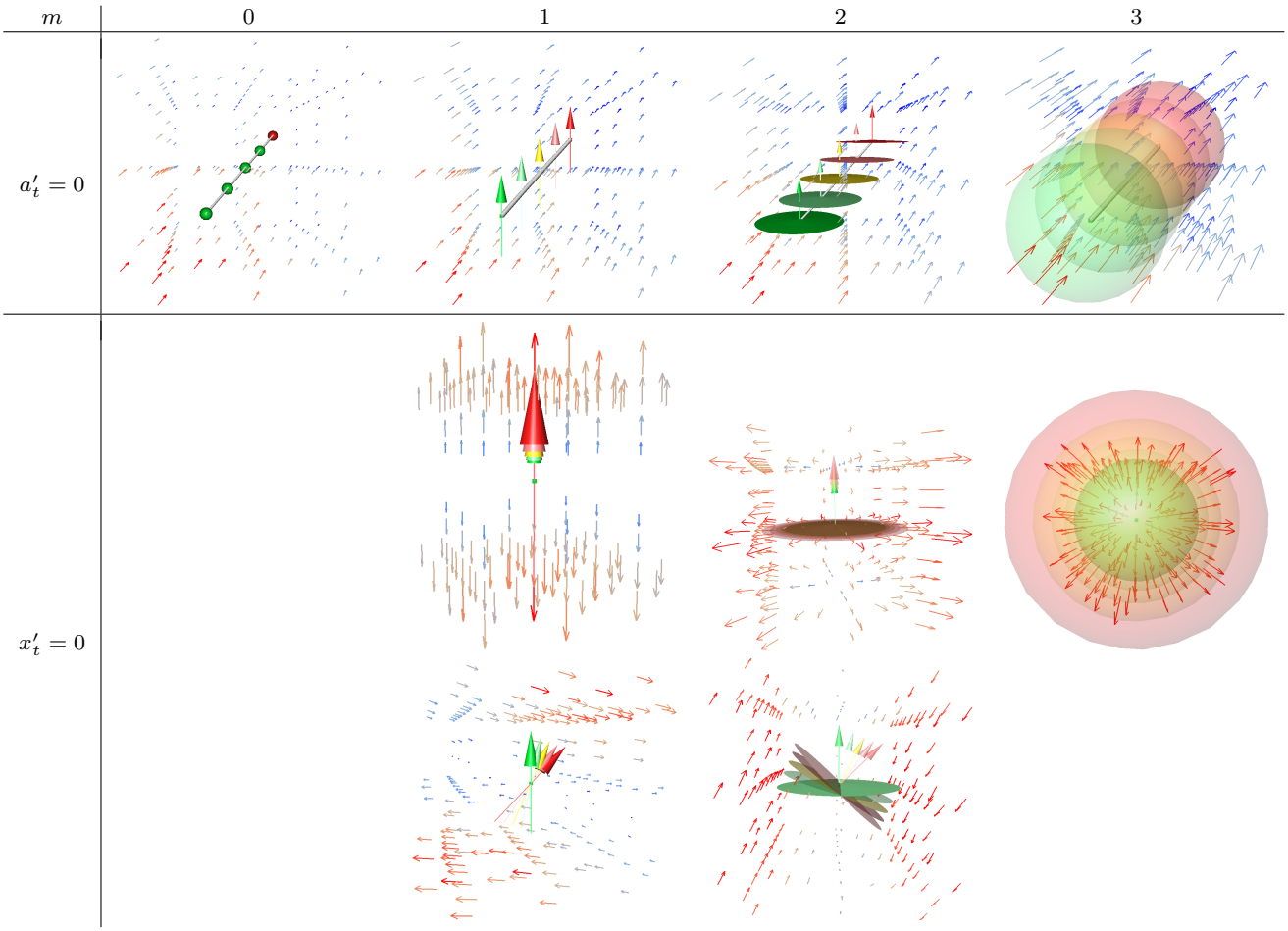

Fig. 2 Temporal evolution of some source Dirac delta m-current $\delta^{a_0}_{x_0}$ (green) under ϕ^v_t towards its target Dirac delta m-current (red) with intermediate timesteps from light green over yellow to light red together with trajectory x_t and wind vectorfield $v_0(\cdot)$

From a practical point of view a simultaneous match of m-currents in a finite range of spectral widths prevents the optimizer to get stuck in some local minimum. The only numerical overhead is the evaluation of the similarity measure at the final time T for all involved scales.

3 Discrete matching problem

3.1 Discretization of the wind by finite elements

In the field of optimal current matching mainly wind discretizations of the form

$$v_t(x) = \sum\nolimits_j k_V(x_{j,t}, x)\alpha_{j,t} \tag{5}$$

have been considered. Here $\alpha_{j,t} \in \mathbb{R}^3$ are the time-dependent momentum vectors and k_V denotes a Gaussian kernel with some global kernel parameter $\sigma_V > 0$, describing the coherent movement of neighboring particles. In order to apply FGT for efficient evaluation, σ_V is necessarily a constant. The vectors $\alpha_{j,t}$ will also be denoted as the *degrees of freedom* (DOF).

It was shown in Joshi and Miller (2000), that the optimal wind which matches a finite set of landmarks to each other is indeed of the form (5). But in practice the global optimum is often not attained. Furthermore the orginal problem in function space (3) could happen to consider infinitly many points. Moreover there is no analogue assertion for the cases $m > 0$. To see this, it suffices to consider the match of the 3-currents δ^1_0 with δ^2_0 as depicted at the bottom of column $m = 3$ of Fig. 2. Clearly, a required local spatial explosion with just one DOF-vector $\alpha_t \in \mathbb{R}^3$ in $v_t(x) = k_V(0, x)\alpha_t$ is insufficient.

The spatial movement of non-compactly supported basis functions along trajectories $x_{j,t}$ may cause numerical difficulties. Too small distances between them cause a redundant or badly conditioned description of the velocity field while the absence of trajectories in a part of the domain produces almost no wind there for

small kernel sizes. The trajectory density varies during optimization and hence is difficult to control. Because the trajectories' starting points are the spatial components of the Dirac delta source currents, the number of trajectories is fixed. Hence, a notion of adaptivity for the velocity field can hardly be introduced. Finally, as mentioned in Sect. 2.2, C^∞ smoothness is not required to solve the evolution equation.

In Risser et al (2010) and Sommer et al (2011), some of the above mentioned drawbacks are overcome by incorporating multiple kernel shapes at different scales σ_V.

Similar to the particle-mesh method proposed in Cotter (2008), we follow a different approach fully decoupling the discretization of the space of m-currents W_m from the spatial velocity space V. Keeping in mind that fast point evaluation of the wind is essential for performance, we consider adaptive hexahedral grids for Ω with hanging nodes saved as an octree. Let us mention that apart from the LDDMM approach the authors Haber et al (2008) have also considered adaptive, multilevel octree grids for image registration with an elastic potential as regularizer. Therein, optimization on difference schemes notably reduce computational time in two and three dimensions. In contrast to Haber et al (2008) we construct either C^1 conforming Hermite finite elements of third order or simpler C^0 conforming Lagrange finite elements of first order over such hexahedral grids. The wind for fixed time $t \in [0,T]$ in the FE basis $\{\varphi_j\}_j$ takes the form

$$v_t(x) = \sum\nolimits_{j=1}^{n} \varphi_j(x)\alpha_{j,t} \ . \tag{6}$$

In contrast to radial basis function discretizations, locally constant functions are contained in the ansatz space and allow to represent local or even global translations with few DOF. Due to the compactly supported basis functions there is no need for an approximate evaluation like FGT with further unknown tolerance parameters. Since the basis functions are fixed in space, the underlying mesh provides a natural clustering which can be exploited via a smart parallel octree search algorithm for point evaluation. Furthermore, this approach provides a multilevel wind hierarchy with a fraction of DOF on the coarsest mesh level completely decoupled from the m-current discretization. These advantages also appear in the particle-mesh method with tensor-products of cubic B-splines for instance. But since we do not apply FFT for wind evaluation, we are more flexible with adaptive meshes and do not require a box domain. Moreover non-constant anisotropic diffusity $\sigma_V(x) \in \mathbb{R}^{3\times 3}$ may be incorporated in future.

A difficulty arises in the computation of $L^2([0,T],V)$ gradients. It involves the solution of a second ($k=1$) or fourth ($k=2$) order elliptic PDE in every time-step and every iteration. It is clear that one should employ suited preconditioners and / or multigrid solvers. Using existing FE libraries limits the implementation overhead. We choose libMesh (Kirk et al 2006), which provides conforming C^1 finite elements on adaptive hexahedral meshes.

All appearing ODEs are numerically integrated using the explicit method of Heun on an equidistant decomposition of the time interval $[0,T]$.

3.2 Current compression and direct evolution

For approximating an m-current $\mathcal{S}^m \in W_m$ as $\hat{\mathcal{S}}^m = \sum_{i=1}^{s_m} \delta_{x_i}^{a_i} \in W_m$ we use the *Orthogonal Matching Pursuit* (OMP) proposed in Durrleman et al (2009). This method iteratively selects the most important points x_i and computes corresponding attributes a_i (i.e. c_i, τ_i, n_i, ρ_i) of a general m-current via a greedy algorithm. It has the advantage of compressing the current information for a characteristic spectral length $\sigma_m > 0$ towards a fraction. This enables the design of highly efficient numerical solution algorithms. The approximation error in OMP is controlled by a threshold parameter and the grid size of a uniform testgrid.

The seeming drawback of loosing the connectivity between vertices (for $m \geq 1$) can be compensated by applying the obtained optimal diffeomorphism to all connected vertices whenever needed. This only requires one additional forward flow computation at the end.

In Sec. 3.2 of Vaillant and Glaunès (2005) two methods to deform a 2-current $\hat{\mathcal{S}}^2$ under a family of diffeomorphisms $(\phi_t^v)_t$ are described. In contrast to all previous work, we will pursue the *direct* approach motivated by Theorem 1. For 2-currents, only one instead of three trajectories is needed to evolve the normal n_0 (Fig. 1). In general, the direct approach requires only one trajectory per attribute, hence decreasing the number of variables in the computation, whereas in the indirect case an artificial m-simplex with $m+1$ vertices is attached.

Remark 3 To quote Rem. 4.13 in Durrleman (2010), the direct evolution of current attributes is closer to the analytical concept of currents and is particularly suited for OMP, where no connectivity between the points is provided. But Durrleman (2010) indicates the need of Jacobi matrices (as they arise in Theorem 1) as a disadvantage for numerical implementation. At least for the gradient computation in the next section we benefit from the simpler structure of v_t in (6), which in Lemma 2 enables easy evaluations of

$$d_{x_t} v_t = \sum\nolimits_{j=1}^{n} \alpha_{j,t} \nabla\varphi_j(x_t)^*$$

and hence $\mathrm{tr}(d_{x_t}v_t)$, $(d_{x_t}v_t)w$ and $(d_{x_t}v_t)^*w$ for a vector $w \in \mathbb{R}^3$. Note that all sums over j are *local* sums due to the compact support of the basis functions φ_j.

3.3 Discrete optimization problem and its gradient

Let $a(\cdot,\cdot)$ denote the bilinear form corresponding to the elliptic differential operator S from (2). We define the sparse symmetric, positive definite matrix $\mathbf{S} := [a(\varphi_i,\varphi_j)]_{i;j=1}^n$ using the FE basis $\{\varphi_j\}_j$ from Sect. 3.1. Moreover, we introduce block vectors $\boldsymbol{\alpha}_t := [\alpha_{i,t}]_{i=1}^n$, $\mathbf{x}_t := \mathbf{x}_t^m := [x_{i,t}]_{i=1}^{s_m}$ and $\mathbf{a}_t := \mathbf{a}_t^m := [a_{i,t}]_{i=1}^{s_m}$. This notation allows to write the matching terms as

$$\begin{aligned} E^m = E^m(\mathbf{x}_T,\mathbf{a}_T) &= \|\phi_T^v(\hat{\mathcal{S}}^m) - \hat{\mathcal{T}}^m\|_{W_m}^2 \\ &= \|\textstyle\sum_{i=1}^{s_m}\delta_{x_{i,T}}^{a_{i,T}} - \sum_{j=1}^{t_m}\delta_{y_j}^{b_j}\|_{W_m}^2 \ . \end{aligned}$$

Finally the discrete form of the current matching problem (3) is

$$\hat{J}(\boldsymbol{\alpha}_t) := \gamma\int_0^T \|v_t(\boldsymbol{\alpha}_t)\|_V^2\,dt + \sum_{m=0}^3 \lambda_m\|\phi_T^v(\hat{\mathcal{S}}^m) - \hat{\mathcal{T}}^m\|_{W_m}^2 \to \min$$

or even shorter via (6) and the relation $\|v_t(\boldsymbol{\alpha}_t)\|_V^2 = a(v_t(\boldsymbol{\alpha}_t), v_t(\boldsymbol{\alpha}_t)) = \boldsymbol{\alpha}_t^*\mathbf{S}\boldsymbol{\alpha}_t$

$$\hat{J}(\boldsymbol{\alpha}_t) = \gamma\int_0^T \boldsymbol{\alpha}_t^*\mathbf{S}\boldsymbol{\alpha}_t\,dt + \sum_{m=0}^3 \lambda_m E^m(\mathbf{x}_T,\mathbf{a}_T) \to \min \ . \tag{7}$$

The analytical computation of the gradient at given $\boldsymbol{\alpha}_t$ becomes manageable though the simpler wind representation (6). Numerically, the computation is more involved due to presence of Hessians of basis functions. But these are easily provided via the already mentioned libMesh library.

Theorem 2 *The gradient of $\hat{J}$ in the L^2-metric is*

$$(\nabla\hat{J})_t = 2\gamma\mathbf{S}\boldsymbol{\alpha}_t + \sum_{m=0}^3 \lambda_m((\boldsymbol{\varphi}_t^m)^*\boldsymbol{\eta}_t^m + (\partial_{\boldsymbol{\alpha}}\mathbf{g}_t^m)^*\boldsymbol{\zeta}_t^m), \tag{8}$$

with

$$\begin{aligned} \boldsymbol{\varphi}_t^m &= [\varphi_j(x_{i,t})I_{d_m}]_{i=1\ldots s_m;j=1\ldots n} \\ \boldsymbol{\zeta}_t^m &= \nabla_{\mathbf{a}_T}E^m + \int_t^T (\partial_{\mathbf{a}}\mathbf{g}_s^m)^*\boldsymbol{\zeta}_s^m\,ds \\ \boldsymbol{\eta}_t^m &= \nabla_{\mathbf{x}_T}E^m + \int_t^T (\partial_{\mathbf{x}}\mathbf{g}_s^m)^*\boldsymbol{\zeta}_s^m\,ds \ . \end{aligned}$$

The proof is postponed to the appendix. The remaining quantities $\nabla_{\mathbf{x}_T}E^m, \nabla_{\mathbf{a}_T}E^m, \partial_{\boldsymbol{\alpha}}\mathbf{g}_t^m, \partial_{\mathbf{x}}\mathbf{g}_t^m$ and $\partial_{\mathbf{a}}\mathbf{g}_t^m$ from Theorem 2 for each m are specified in the next two lemmas.

Lemma 1 *Let*

$$f_m(x) = \textstyle\sum_{i=1}^{s_m} k_m(x_{i,T},x)a_{i,T} - \sum_{j=1}^{t_m} k_m(y_j,x)b_j \ .$$

There hold

$$\begin{aligned} &\nabla_{\mathbf{x}_T}E^m = [2(d_{x_{i,T}}f_m(x_{i,T}))^*a_{i,T}]_{i=1}^{s_m} \quad \textit{and} \\ &\nabla_{\mathbf{a}_T}E^m = [2f_m(x_{i,T})]_{i=1}^{s_m} \ . \end{aligned}$$

Proof

$$\begin{aligned} (\partial_{x_T}E^m)\eta &= 2\left[\left(\partial_{x_T}\textstyle\sum_{i=1}^{s_m}\delta_{x_{i,T}}^{a_{i,T}}\right)\eta\right](f_m) \\ &= 2a_T^*\left(d_{x_T}f_m(x_T)\right)\eta \\ \nabla_{x_T}E^m &= 2(d_{x_T}f_m(x_T))^*a_T \\ &= 2\Big(\textstyle\sum_{i=1}^{s_m}(\nabla_2 k_m(x_{i,T},x_T))a_{i,T}^* \\ &\quad - \sum_{j=1}^{t_m}(\nabla_2 k_m(y_j,x_T))b_j^*\Big)a_T \\ (\partial_{a_T}E^m)\eta &= 2\left[\left(\partial_{a_T}\textstyle\sum_{i=1}^{s_m}\delta_{x_{i,T}}^{a_{i,T}}\right)\eta\right](f_m) \\ &= 2\eta^* f_m(x_T) \ . \end{aligned}$$

□

Lemma 2 *For $\mathbf{g}_t^m$ in (12) their sparse Jacobians are given via*

$$\begin{aligned} \mathbf{g}_t^0 &= \mathbf{0} \\ \partial_{\boldsymbol{\alpha}}\mathbf{g}_t^1 &= \left[(\tau_{i,t}^*\nabla\varphi_j(x_{i,t}))I_3\right]_{i=1\ldots s_1;j=1\ldots n} \\ \partial_{\boldsymbol{\alpha}}\mathbf{g}_t^2 &= \left[n_{i,t}\nabla\varphi_j(x_{i,t})^* - \nabla\varphi_j(x_{i,t})n_{i,t}^*\right]_{i=1\ldots s_2;j=1\ldots n} \\ \partial_{\boldsymbol{\alpha}}\mathbf{g}_t^3 &= \left[\rho_{i,t}\nabla\varphi_j(x_{i,t})^*\right]_{i=1\ldots s_3;j=1\ldots n} \\ \partial_{\mathbf{x}}\mathbf{g}_t^1 &= \mathrm{diag}\Big[\textstyle\sum_{j=1}^n \alpha_{j,t}\tau_{i,t}^* H_{\varphi_j}(x_{i,t})\Big]_{i=1}^{s_1} \\ \partial_{\mathbf{x}}\mathbf{g}_t^2 &= \mathrm{diag}\Big[\textstyle\sum_{j=1}^n n_{i,t}(\alpha_{j,t}^* H_{\varphi_j}(x_{i,t})) - (\alpha_{j,t}^* n_{i,t})H_{\varphi_j}(x_{i,t})\Big]_{i=1}^{s_2} \\ \partial_{\mathbf{x}}\mathbf{g}_t^3 &= \mathrm{diag}\Big[\textstyle\sum_{j=1}^n \rho_{i,t}\alpha_{j,t}^* H_{\varphi_j}(x_{i,t})\Big]_{i=1}^{s_3} \\ \partial_{\boldsymbol{\tau}}\mathbf{g}_t^1 &= \mathrm{diag}\Big[\textstyle\sum_{j=1}^n \alpha_{j,t}\nabla\varphi_j(x_{i,t})^*\Big]_{i=1}^{s_1} \\ \partial_{\mathbf{n}}\mathbf{g}_t^2 &= \mathrm{diag}\Big[\textstyle\sum_{j=1}^n (\alpha_{j,t}^*\nabla\varphi_j(x_{i,t}))I_3 - \nabla\varphi_j(x_{i,t})\alpha_{j,t}^*\Big]_{i=1}^{s_2} \\ \partial_{\boldsymbol{\rho}}\mathbf{g}_t^3 &= \mathrm{diag}\Big[\textstyle\sum_{j=1}^n \alpha_{j,t}^*\nabla\varphi_j(x_{i,t})\Big]_{i=1}^{s_3}, \end{aligned}$$

where $H_{\varphi_j}(x_{i,t})$ denote the Hessian of φ_j at $x_{i,t}$.

Proof The proof for all cases of m can easily be adapted from the case $m = 2$. For this choice the derivatives of $\mathbf{g}_t^2$ follow from direct calculations starting with

$$\begin{aligned} \mathbf{g}_t^2 &= \mathbf{g}^2(\boldsymbol{\alpha}_t,\mathbf{x}_t,\mathbf{n}_t) \\ &= \mathrm{diag}\left[\mathrm{tr}(d_{x_{i,t}}v_t)I_3 - (d_{x_{i,t}}v_t)^*\right]_{i=1}^{s_2}\mathbf{n}_t \\ &= \mathrm{diag}\Big[\textstyle\sum_{j=1}^n (\alpha_{j,t}^*\nabla\varphi_j(x_{i,t}))I_3 - \nabla\varphi_j(x_{i,t})\alpha_{j,t}^*\Big]_{i=1}^{s_2}\mathbf{n}_t \\ &= \Big[\textstyle\sum_{j=1}^n n_{i,t}(\alpha_{j,t}^*\nabla\varphi_j(x_{i,t})) - \nabla\varphi_j(x_{i,t})(\alpha_{j,t}^* n_{i,t})\Big]_{i=1}^{s_2}, \end{aligned}$$

where $\mathrm{diag}[\mathbf{v}] = [\delta_{ij}v_i]_{i;j=1}^s$ for $\mathbf{v} \in \mathbb{R}^s$ and δ_{ij} denotes the Kronecker delta. □

Table 2 Summary of involved parameters for all four numerical experiments

Ex.	1	2	3	4
data	pelvis			mandible
m	0	1	0, 1, 3	0, 1, 2
d_Ω	541	495	534	220
σ_{comp}	8	3	5	2
s_m	1746	1084	33,652, 7390	19,497,4385
t_m	2141	1286	33,772,10000	19,455,4236
$\tilde{\lambda}_m$	1	1	4, 2, 0.02	3, 1, 1
Σ	8	3,10,17,24	5, 13, 21, 29	10, 20, 30, 40
σ_V	C^0: 100, C^1: 15			10

Corollary 1 *If $\lambda_m = 0$ for $m > 0$ Theorem 2 simply provides*

$$(\nabla \hat{J})_t = 2\gamma \mathbf{S}\boldsymbol{\alpha}_t + \lambda_0(\boldsymbol{\varphi}_t^0)^* \nabla_{\mathbf{x}_T} E^0 \ .$$

Remark 4 The $L^2([0,T],V)$-gradient of $\hat{J}$ is immediately obtained by applying $\mathbf{S}^{-1}$ from the left in equation (8).

4 Numerical experiments

As a first example we are going to solve the discrete optimization problem (7) in order to compare our results with the software ExoShape [1] where C^∞ wind of the form (5) is implemented. Next, we consider three examples of the discrete analogon to the extended problem (4) with multiple spectral widths in the similarity measure.

The first three examples look at various correspondence problems in terms of different m cases between two pelvic bones, while the last one considers two mandible bones together with their alveolar nerves. [2]

An overview about the actual m-cases and the associated parameters can be gained from Tab. 2. To get an insight onto the absolute scale of each problem, we report $d_\Omega = \text{diam}(\Omega)$ in terms of millimeter units. The row σ_{comp} lists the spectral width of the Gaussian kernel, at which the OMP to the involved lines, surfaces and volumes is applied. The resulting discrete currents $\hat{\mathcal{S}}^m$ and $\hat{\mathcal{T}}^m$ are sums of s_m and t_m Dirac m-currents respectively. When matching different m-cases simultaneously the user has to provide suitable weights λ_m in the objective $\hat{J}$. But due to different scaling of each RKHS-norm and in order to obtain $\mathcal{O}(1)$ numbers in the objective it is reasonable to define the relative weights

$$\tilde{\lambda}_m = \lambda_m \cdot \|\hat{\mathcal{S}}^m - \hat{\mathcal{T}}^m\|^2_{W_m(\sigma_{m,0})},$$

where $\sigma_{m,0}$ denotes the smallest spectral width in Σ_m. We consider only one finite set Σ of kernel sizes independently from m.

All problems are solved six times for different wind discretizations: For Lagrange FE C^0 wind ($k = 1$) and for Hermite FE C^1 wind ($k = 2$) either on a coarse uniform or an adaptive, or a fine uniform hexahedral mesh. We simply mark cells for refinement, whenever a point x_i from the compressed m-currents $\hat{\mathcal{S}}^m$ or $\hat{\mathcal{T}}^m$ is contained therein. Let us comment on the last row of Tab. 2 documenting the values σ_V from (2). These manually adjusted numbers have impact on the spatial smoothness of C^0 and C^1 wind and scale with the bounding box of the domain. Although we choose $\gamma = 0$ for all experiments, the discrete operator $\mathbf{S}$ is still present when optimizing with the $L^2([0,T],V)$-gradient as remarked in the last section.

In the tables Tab. 3-6 the column DOF denotes the number of freely choosable vectors $\alpha_{j,t}$ for fixed t. On adaptive meshes, vectors $\alpha_{j,t}$ on hanging nodes are not freely choosable. They have to satisfy a global C^0 or C^1 condition. For $k = 1$ there is one FE basis function per node, while for $k = 2$ we have eight. In the last column we document the objective $\hat{J}$. In the remaining columns we additionally report distance measures which allow a direct geometric interpretation in millimeters. These are the mean, standard deviation, root mean square and the maximum of the one sided distance function from the deformed source (in the first rows) and from the undeformed source (in the last row) towards the target.

In the following figures Fig. 3-19 the color green encodes sources $\mathcal{S}^m$ or $\hat{\mathcal{S}}^m$ (at time $t = 0$), while the color red is for targets $\mathcal{T}^m$ or $\hat{\mathcal{T}}^m$ (at time $t = T$). Intermediate colors from light green over yellow to light red correspond to intermediate times from 0 to T. In general, black or gray colors stand for deformed sources $\mathcal{S}_T^m$ or $\hat{\mathcal{S}}_T^m$ (at time $t = T$).

4.1 Example 1: Pelvic bone ($m = 0$)

We consider the case $m = 0$. The surfaces $\mathcal{S}^2$ and $\mathcal{T}^2$ of two pelvic bones are depicted in Fig. 3. To both surface densities we apply the OMP towards $\hat{\mathcal{S}}^0$ and $\hat{\mathcal{T}}^0$ which are sketched as set of spheres of diameter 8 in Fig. 4.

Starting from a uniform hexahedral grid with $6 \cdot 4 \cdot 5 = 120$ nodes we refine cells containing the points x_i from $\hat{\mathcal{S}}^0$ and $\hat{\mathcal{T}}^0$. The resulting hexahedral adaptive grid

[1] `http://www-sop.inria.fr/asclepios/projects/Health-e-Child/ShapeAnalysis/`

[2] Pelvic bone data by courtesy of Markus Heller, Julius Wolff Institute and Center for Musculoskeletal Surgery Charité-Universitätsmedizin Berlin, Germany. Mandible data by courtesy of Max Zinser, Universitätsklinikum Köln, Germany.

Fig. 3 Pelvic bone surfaces $\mathcal{S}^2$ (green), $\mathcal{T}^2$ (red) for Ex. 1

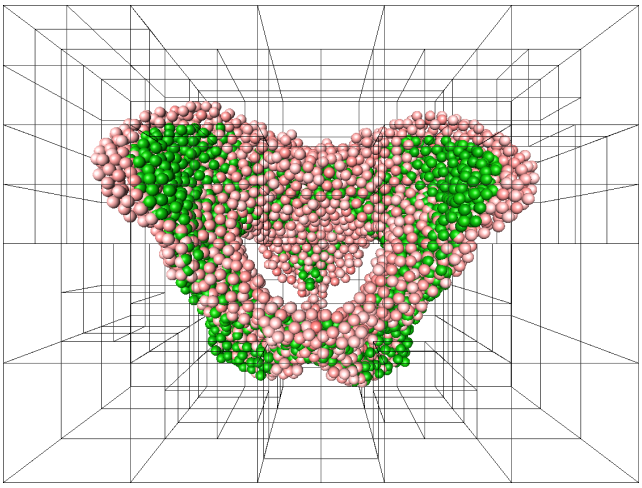

Fig. 4 Compressed 0-currents $\hat{\mathcal{S}}^0$ and $\hat{\mathcal{T}}^0$ for spectral width $\sigma_0 = 8$ depicted as $s_0 = 1746$ green and $t_0 = 2141$ red spheres of diameter 8 together with the adaptive grid consisting of 523 nodes (164 of them are hanging nodes) for Ex. 1

with 523 nodes (164 of them are hanging nodes) is also depicted in Fig. 4.

The deformed pelvic bone surfaces $\mathcal{S}_T^2$ are displayed for adaptive C^0 wind in Fig. 5 and for adaptive C^1 wind in Fig. 6. Finally in Fig. 7 we compare our results with the software ExoShape, generating C^∞ wind via ansatz (5) with $\sigma_V = 30$. The grayscale visualizes the term $\mathrm{dist}_{x\in\mathcal{S}_T^2}(x, \mathcal{T}^2)$. One should keep in mind, that with $\gamma = 0$ the deformation norm vanishes in the example, but different differential operators are still present for velocity field evaluation. Although a proper comparison between all methods should use the same deformation norm $\|\cdot\|_V$, Exoshape does not easily support its change. Additionally in the lower left corner distance histograms over the surface are displayed.

A quantitative comparison between all different discretizations for the wind field is given in Tab. 3. All methods provide acceptable matches with respect to the fixed level of detail $\sigma_0 = 8$. Especially the surface $\mathcal{S}_T^2$ corresponding to adaptive C^1 wind is also visually

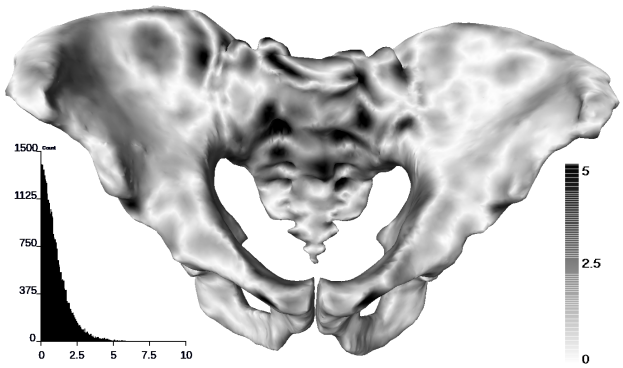

Fig. 5 Deformed $\mathcal{S}_T^2$ under adaptive C^0 wind for Ex. 1

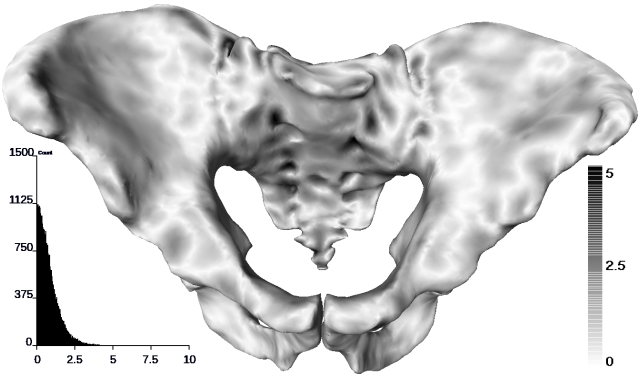

Fig. 6 Deformed $\mathcal{S}_T^2$ under adaptive C^1 wind for Ex. 1

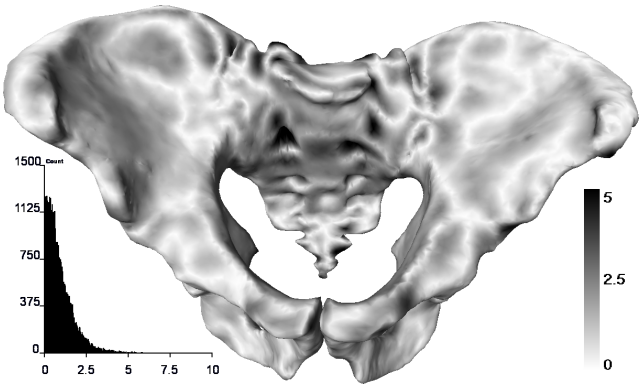

Fig. 7 Deformed $\mathcal{S}_T^2$ under C^∞ wind for Ex. 1

Table 3 One-sided surface distances between deformed pelvic bone $\mathcal{S}_T^2$ and target bone $\mathcal{T}^2$ for Ex. 1

v_t		DOF	mean	stddev	rms	max	$\hat{J}$
C^0	uniform	120	1.52	1.53	2.16	14.99	0.23
C^0	adaptive	359	1.06	1.06	1.50	10.94	0.17
C^0	uniform	693	1.04	1.05	1.48	10.40	0.16
C^1	uniform	960	1.00	0.94	1.37	9.41	0.15
C^1	adaptive	2872	0.81	0.73	1.09	7.29	0.12
C^1	uniform	5544	0.81	0.73	1.09	7.32	0.11
C^∞		1746	0.97	0.93	1.34	9.70	0.11
$\mathrm{dist}_{x\in\mathcal{S}^2}(x, \mathcal{T}^2)$			5.08	3.87	6.39	21.05	1.00

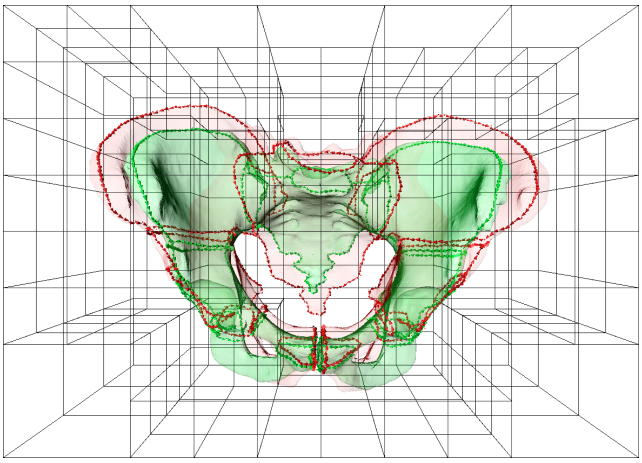

Fig. 8 Compressed 1-currents $\hat{\mathcal{S}}^1$ and $\hat{\mathcal{T}}^1$ for spectral width $\sigma_1 = 3$ depicted as $s_1 = 1084$ green and $t_1 = 1286$ red arrows in their pelvic bone context together with the adaptive grid consisting of 554 nodes (147 of them are hanging nodes) for Ex. 2

closest to $\mathcal{T}^2$. Generally, we observe higher matching accuracy for increasing numbers of DOF. The uniform C^1 wind with 960 DOF is competetive to ExoShape with 1746 DOF. Adaptive C^1 is even better, but also has more DOF. Remarkable is the fact that there is almost no difference between adaptive C^{k-1} and globally refined C^{k-1} wind although we have used a quite simple and heuristic refinement strategy.

4.2 Example 2: Pelvic bone ($m = 1$)

By looking at anatomic feature lines (e.g. of salient curvature) on the the surface of pelvic bones we consider the case $m = 1$. These directed lines $\mathcal{S}^1$ and $\mathcal{T}^1$ are sketched as green and red arrows in Fig. 8 after applying the OMP.

We solve the extended discrete matching problem of (4). The solution for C^1 wind ($k = 2$) on the adaptive grid is shown in Fig. 9. This computation shows the practicability of our method for a non-trivial case $m > 0$, where also the attributes τ_i evolve under the time-dependent wind field. On most areas the matching accuracy is sufficient with respect to the initially chosen geometric level of detail in the compression. It is clear that in areas of nonsatisfying match a local grid refinement and hence more local DOF for the wind should follow. On the other hand, a-priori refinement in areas of initially satisfying local fit is not required.

Tab. 4 lists the one-sided line distances between deformed lineset $\mathcal{S}^1_T$ and target $\mathcal{T}^1$ for all six wind scenarios. Our observations are similar as for the $m = 0$ case: the more wind DOF, the better the match. In terms of accuracy adaptive refinement is competitive to

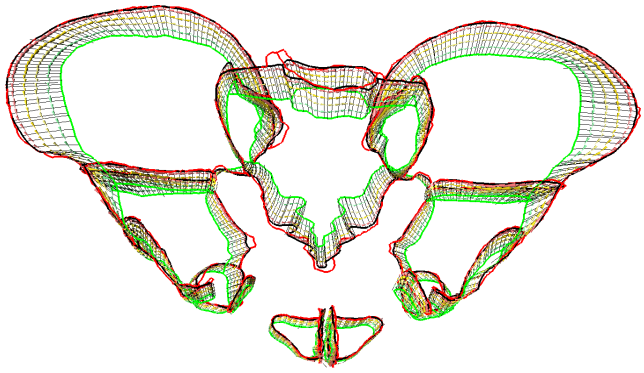

Fig. 9 Green source $\mathcal{S}^1$, red target $\mathcal{T}^1$ and black deformed source lineset $\mathcal{S}^1_T$ for adaptive C^1 wind together with trajectories $x_{i,t}$ and intermediate light green to light red tangents $\tau_{i,t}$ for Ex. 2

Table 4 One-sided line distances between deformed lineset $\mathcal{S}^1_T$ and target lineset $\mathcal{T}^1$ for Ex. 2

v_t		DOF	mean	stddev	rms	max	$\hat{J}$
C^0	uniform	120	2.61	2.45	3.58	20.31	2.13
C^0	adaptive	407	1.69	1.67	2.37	14.21	1.45
C^0	uniform	693	1.71	1.75	2.45	15.84	1.49
C^1	uniform	960	1.38	1.31	1.90	9.19	1.35
C^1	adaptive	3256	1.11	1.22	1.65	9.96	1.10
C^1	uniform	5544	1.11	1.22	1.65	9.99	1.10
$\mathrm{dist}_{x\in\mathcal{S}^1}(x,\mathcal{T}^1)$			10.41	6.31	12.17	30.18	6.75

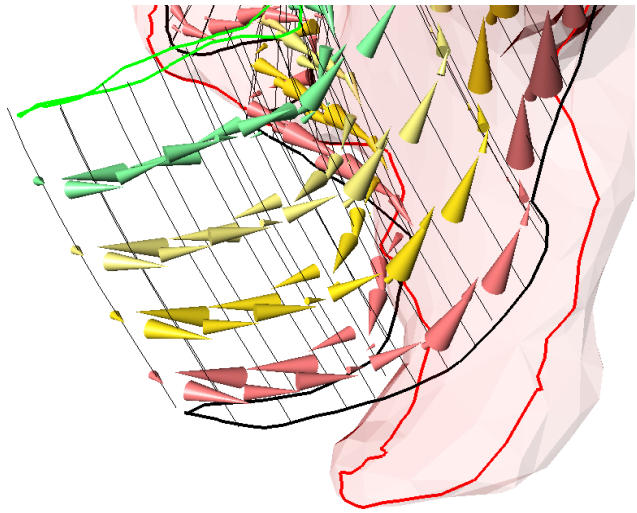

Fig. 10 Zoom at sacrum area for adaptive C^1 wind with trajectories $x_{i,t}$ and intermediate light green to light red tangents $\tau_{i,t}$ for Ex. 2

global uniform refinement. However the match near the sacrum shown in Fig. 10 is not acceptable with respect to the considered geometric level of detail. This fact is also reflected in Tab. 4, where the maximal one-sided distance between deformed line $\mathcal{S}^1_T$ and $\mathcal{T}^1$ is about 10. At tips like in the sacrum-area, back and forth tangents almost cancel out at large scales, while on small scales

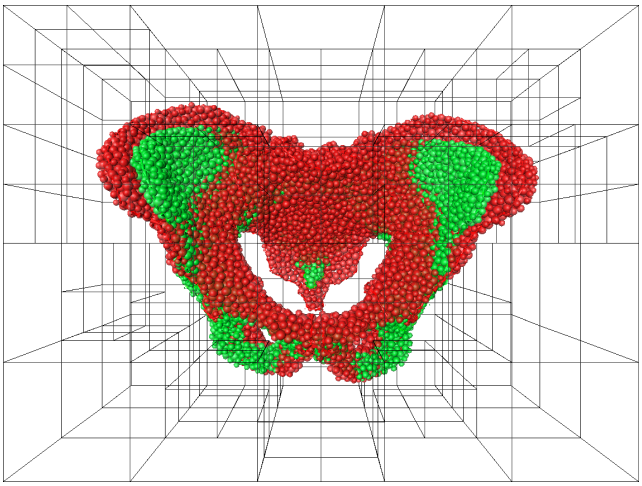

Fig. 11 Compressed 3-currents $\hat{\mathcal{S}}^3$ and $\hat{\mathcal{T}}^3$ for spectral width $\sigma = 5$ depicted as $s_3 = 7390$ green and $t_3 = 10000$ red balls of volume ρ_i together with the adaptive grid consisting of 523 nodes (164 of them are hanging nodes) for Ex. 3

source and target sacrum line do not correlate in the similarity measure due to their large distance. Therefore we also match undirected scalar information in the following

4.3 Example 3: Pelvic bone ($m = 0, 1, 3$)

Let us consider the case $m = 0$, $m = 1$ and $m = 3$ simultaneously. We manually mark 33 points on both source and target pelvic bones, set all their attributes $c_i = 1$ and consider them as 0-currents. In particular, the tip of each sacrum is selected. Additionally we consider the pelvic bones as filled volumetric bodies, i.e. as 3-currents. Their compression delivers discrete 3-currents $\hat{\mathcal{S}}^3$ and $\hat{\mathcal{T}}^3$ visualized in Fig. 11 as green and red balls of volume ρ_i together with the adaptive grid with 523 nodes. Since we have manually selected points in the $m = 0$ case, we enforce a rather good match, which is reflected in the large relative weight $\tilde{\lambda}_0 = 4$.

We exemplarily depict the solution in terms of the gray deformed pelvic bone $\mathcal{S}_T^2$ for adaptive C^1 wind in Fig. 12 and set it into the context with source (green), deformed (black) and target (red) points and lines. In Fig. 13 the pushforward of the source 3-current $\hat{\mathcal{S}}^3$ under the map ϕ_t^v for multiple times starting from $t = 0$ in green to $t = T$ in light red is shown.

The one-sided distances to the target pelvic bone for all six optimal solutions are collected in Tab. 5. We notice that the maximum of the distance function is - as intended - not realized at the sacrum area anymore. A comparison between the Figs. 10 and 14 shows indeed the improvement due to the manually selected points and the higher weight $\tilde{\lambda}_0$. Both cases in k reveal, that

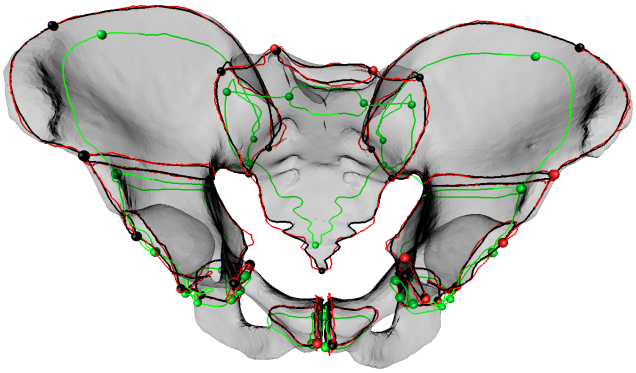

Fig. 12 Green source points $\mathcal{S}^0$ and lineset $\mathcal{S}^1$, red target points $\mathcal{T}^0$ and lineset $\mathcal{T}^1$ and black deformed points $\mathcal{S}_T^0$ and lineset $\mathcal{S}_T^1$ for adaptive C^1 wind together with gray deformed pelvic bone $\mathcal{S}_T^2$ for Ex. 3

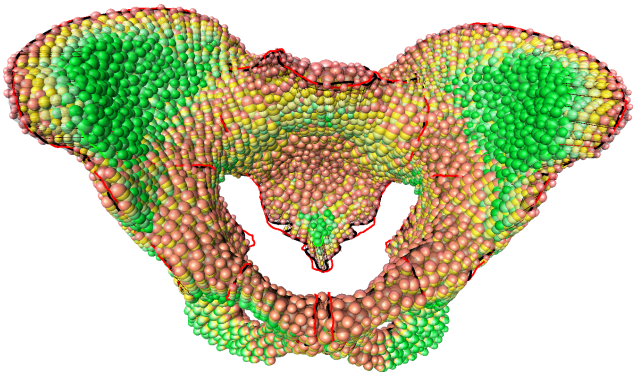

Fig. 13 Green source 3-current $\hat{\mathcal{S}}^3$ towards light red deformed 3-current $\hat{\mathcal{S}}_T^3$ for adaptive C^1 wind together with trajectories $x_{i,t}$ and intermediate light green over yellow balls of volumes $\rho_{i,t}$ for Ex. 3

Table 5 One-sided surface distances between deformed pelvic bone $\mathcal{S}_T^2$ and target bone $\mathcal{T}^2$ for Ex. 3

v_t		DOF	mean	stddev	rms	max	$\hat{J}$
C^0	uniform	120	2.46	2.31	3.38	20.04	7.00
C^0	adaptive	359	2.33	2.06	3.11	17.92	3.89
C^0	uniform	693	2.30	2.08	3.11	17.59	3.71
C^1	uniform	960	2.11	1.92	2.85	17.91	3.16
C^1	adaptive	2872	2.24	2.12	3.08	17.39	2.34
C^1	uniform	5544	2.24	2.12	3.09	17.49	2.32
$\mathrm{dist}_{x\in\mathcal{S}^2}(x, \mathcal{T}^2)$			5.08	3.87	6.39	21.05	19.98

adaptivity pays off: We obtain almost the same matching accuracy with substantially less DOF compared to the global refined case. It is clear that for improving the match, further local mesh refinement is required. This leads to a local enrichment of the FE space for the wind field.

Fig. 14 also displays a zoom into the temporal evolution of the family of discrete 3-currents $(\sum \delta_{x_{i,t}}^{\rho_{i,t}})_t$ in terms of spheres at $x_{i,t}$ of volume $\rho_{i,t}$. Again the color encodes the time from green ($t = 0$) to light red ($t = T$).

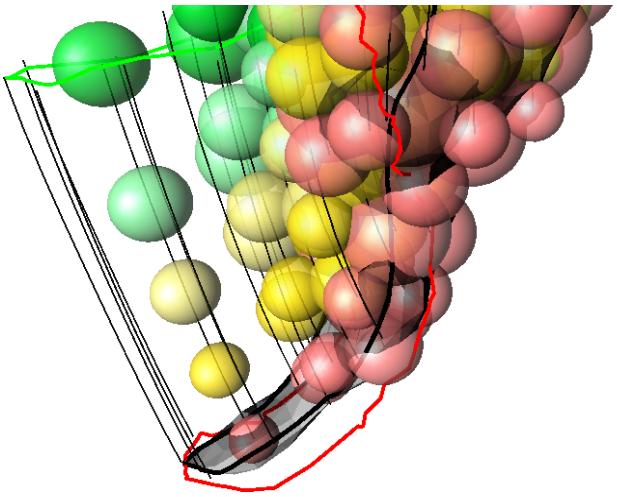

Fig. 14 Zoom at sacrum area for adaptive C^1 wind with trajectories $x_{i,t}$ and intermediate light green to light red balls of volumes $\rho_{i,t}$ together with the linesets $\mathcal{S}^1$ (green), $\mathcal{S}_T^1$ (black) and $\mathcal{T}^1$ (red) for Ex. 3

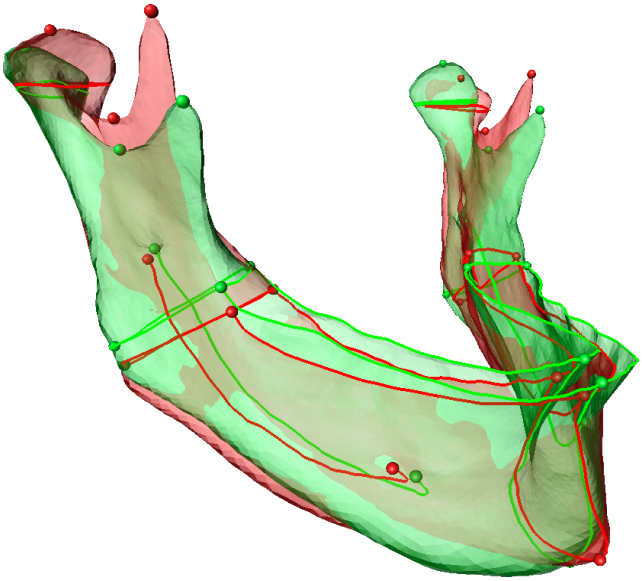

Fig. 15 Green source mandible bone $\mathcal{S}^2$ with charactertic lines and nerves $\mathcal{S}^1$ and $s_0 = 19$ points considered as 0-current $\hat{\mathcal{S}}^0$ together with its red target counterparts for Ex. 4

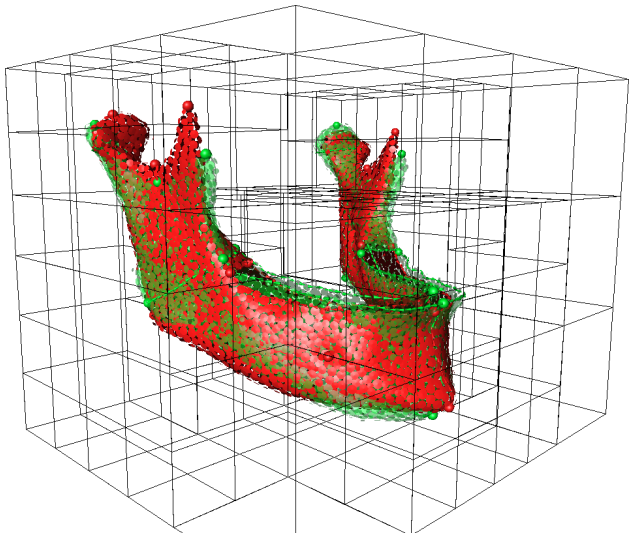

Fig. 16 The discrete counterpart to Fig. 15 after the OMP together with the adaptive grid having 332 nodes for Ex. 4

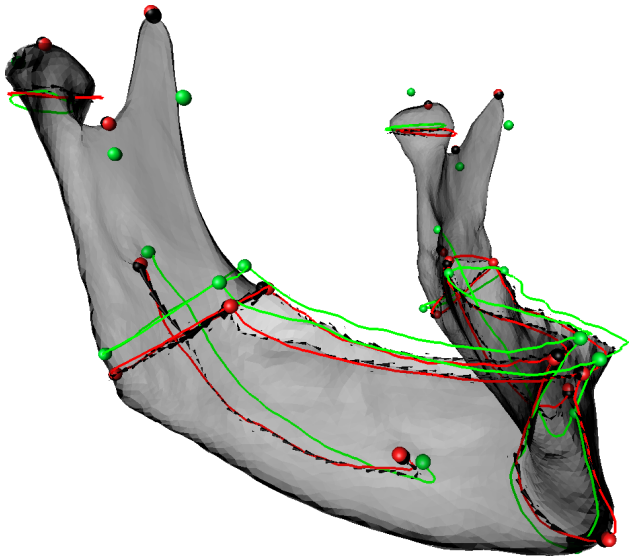

Fig. 17 Green source points $\mathcal{S}^0$ and lineset $\mathcal{S}^1$, red target points $\mathcal{T}^0$ and lineset $\mathcal{T}^1$ and black deformed points $\hat{\mathcal{S}}_T^0$ and 1-current $\hat{\mathcal{S}}_T^1$ for adaptive C^1 wind together with gray deformed mandible bone $\mathcal{S}_T^2$ for Ex. 4

4.4 Example 4: Mandible bone ($m = 0, 1, 2$)

It remains to demonstrate an example for evolving $m =$ 2-currents. We consider two mandible bones without the teeth area as surfaces together with their alveolar nerves and other feature lines ($m = 1$) of salient curvature. Additionally we manually mark 19 points on the surfaces and lines, attach colors $c_i = 1$ to them and consider these $\hat{\mathcal{S}}^0$, $\hat{\mathcal{T}}^0$ as 0-currents. The exact geometric situation is depicted in Fig. 15.

The result after the OMP with $\sigma_{\text{comp}} = 2$ is shown in Fig. 16 together with the adaptive grid.

Besides the deformed mandible bone $\mathcal{S}_T^2$ in gray Fig. 17 displays also the deformed 1-current $\hat{\mathcal{S}}_T^1$ in black. Especially the correspondence of the points but also between the nerves are found up to an acceptable accuracy.

Displaying the direct temporal evolution of discrete 2-currents is part of Fig. 18 and Fig. 19. The meaning of the colors is analogous to the Figs. 13 and 14 from Ex. 3.

For completeness we show the numbers for all six spatial wind discretizations in Tab. 6. We observe the same trends as in the previous examples.

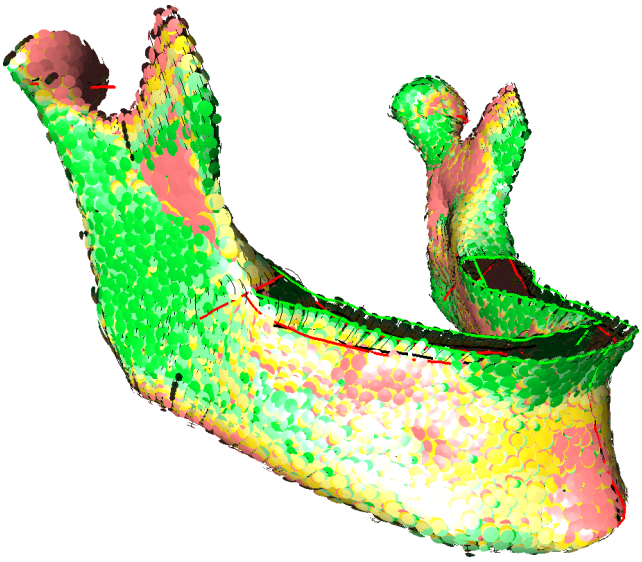

Fig. 18 Green source 2-current $\hat{\mathcal{S}}^2$ towards light red deformed 2-current $\hat{\mathcal{S}}_T^2$ for adaptive C^1 wind together with trajectories $x_{i,t}$ and intermediate light green over yellow circles of area $|n_{i,t}|$ for Ex. 4

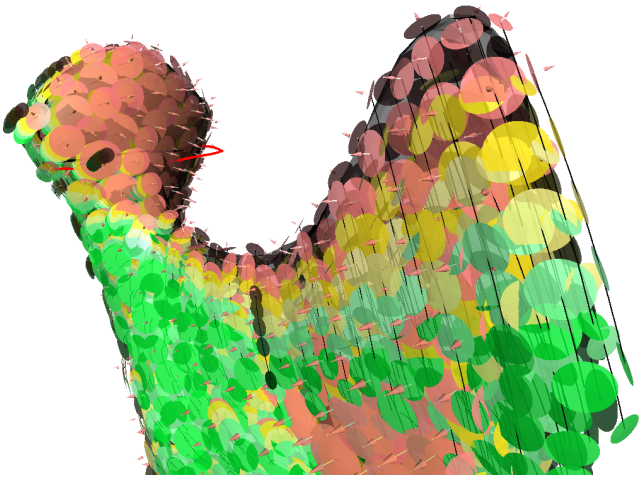

Fig. 19 Zoom at mandibular joint for adaptive C^1 wind with trajectories $x_{i,t}$ and intermediate light green to light red circles of area $|n_{i,t}|$ together with the light red normals $n_{i,T}$ for Ex. 4

Table 6 One-sided surface distances between deformed mandible bone $\mathcal{S}_T^2$ and target bone $\mathcal{T}^2$ for Ex. 4

v_t		DOF	mean	stddev	rms	max	$\hat{J}$
C^0	uniform	80	0.78	0.73	1.07	5.91	2.49
C^0	adaptive	234	0.72	0.62	0.95	4.47	2.55
C^0	uniform	441	0.66	0.54	0.85	4.10	1.89
C^1	uniform	640	0.61	0.50	0.79	4.13	1.18
C^1	adaptive	1872	0.52	0.43	0.68	2.96	0.96
C^1	uniform	3528	0.51	0.42	0.66	2.93	0.95
$\mathrm{dist}_{x\in\mathcal{S}^2}(x,\mathcal{T}^2)$			1.33	1.10	1.72	5.75	8.91

Conclusion

We present a unified treatment of matching m-currents ($m = 0, 1, 2, 3$) in the framework of LDDMM. Two new key aspects are developed:

On the one hand we consistently apply C^1 conforming AFEM for generating diffeomorphisms of the embedded space. In practice, it turned out that also C^0 conforming Lagrangian AFEM are suited. They are still able to compute locally smooth one-to-one correspondences, but are easier to implement and generate smaller discrete systems to solve. The main advantage of using AFEM lies in the fixed spatial clustering and spatial flexibility. The non-moving compactly supported basis functions further simplify analytical and numerical gradient computations.

On the other hand we directly morph the discrete current attributes obtained from the Orthogonal Matching Pursuit algorithm. This approach is closer to the context of currents and requires less trajectories and hence less memory during the optimization process. Its seeming drawback of loosing connectivity information can be compensated by applying the found optimal deformation map to the original connected set.

In future we focus on reliable a-posteriori error estimators in time and space steering the adaptive refinement process for the velocity field. Moreover we hope to benefit from some multilevel, hierarchic wind structure, which is natural to consider over nested grids. Furthermore, it is now possible to consider non-constant spatial diffusity $0 < \sigma_V(x) \in L^\infty(\Omega)^{3\times 3}$ in the operator L^*L providing more local flexibility whenever required for matching.

Acknowledgements We thank Stanley Durrleman from the University of Utah for the fruitful discussion and helpful suggestions at the initial phase of this paper. We further acknowledge support by DFG-MATHEON Project F2. We thank Malik Kirchner for implementing parts of the required tools.

References

Beg MF, Miller MI, Trouvé A, Younes L (2005) Computing large deformation metric mappings via geodesic flows of diffeomorphisms. International Journal of Computer Vision 61(2):139–157, DOI 10.1023/B:VISI.0000043755.93987.aa

Burger M, Ruthotto L, Modersitzki J (2011) A hyperelastic regularization energy for image registration. Preprint, WWU Münster

Cao Y, Miller MI, Winslow RL, Younes L (2005) Large deformation diffeomorphic metric mapping of vector fields. IEEE Transactions on Medical Imaging 24(9):1216–1230

Cotter C (2008) The variational particle-mesh method for matching curves. Journal of Physics A: Mathematical and Theoretical 41(34):344,003

Dupuis P, Grenander U, Miller MI (1998) Variational problems on flows of diffeomorphisms for image matching. Q Appl Math 56(3):587–600

Durrleman S (2010) Statistical models of currents for measuring the variability of anatomical curves, surfaces and their evolution. Thèse de sciences (phd thesis), Université de Nice-Sophia Antipolis

Durrleman S, Pennec X, Trouvé A, Ayache N (2009) Statistical models of sets of curves and surfaces based on currents. Medical Image Analysis 13(5):793–808, DOI 10.1016/j.media.2009.07.007, includes Special Section on the 12th International Conference on Medical Imaging and Computer Assisted Intervention

Federer H (1996) Geometric measure theory. Repr. of the 1969 ed. Classics in Mathematics. Berlin: Springer-Verlag

Glaunès J (2005) Transport par difféomorphismes de points, de mesures et de courants pour la comparaison de formes et l'anatomie numérique. PhD thesis, Université Paris 13

Glaunès J, Trouvé A, Younes L (2004) Diffeomorphic matching of distributions: a new approach for unlabelled point-sets and sub-manifolds matching. In: Proceedings of the 2004 IEEE computer society conference on Computer vision and pattern recognition, Washington, DC, USA, CVPR'04, vol 2, pp 712–718, DOI 10.1109/CVPR.2004.1315234

Glaunès J, Qiu A, Miller MI, Younes L (2008) Large deformation diffeomorphic metric curve mapping. International Journal of Computer Vision 80(3):317–336, DOI 10.1007/s11263-008-0141-9

Haber E, Heldmann S, Modersitzki J (2008) Adaptive mesh refinement for nonparametric image registration. SIAM Journal on Scientific Computing 30(6):3012–3027, DOI 10.1137/070687724

Joshi SC, Miller MI (2000) Landmark matching via large deformation diffeomorphisms. IEEE Transactions on Image Processing 9(8):1357–1370, DOI 10.1109/83.855431

Kirk BS, Peterson JW, Stogner RH, Carey GF (2006) `libMesh`: A C++ Library for Parallel Adaptive Mesh Refinement/Coarsening Simulations. Engineering with Computers 22(3–4):237–254

Marsland S, Twining C (2004) Constructing diffeomorphic representations for the groupwise analysis of non-rigid registrations of medical images. IEEE Transactions on Medical Imaging 23(8):1006–1020

Mattheij RM, Molenaar J (2002) Ordinary differential equations in theory and practice. Reprint of the 1996 original. Classics in Applied Mathematics. SIAM

Morgan F (2009) Geometric measure theory. A beginner's guide. 4th ed. Elsevier

Morita S (2001) Geometry of differential forms. American Mathematical Society

Risser L, Vialard FX, Wolz R, Holm DD, Rueckert D (2010) Simultaneous fine and coarse diffeomorphic registration: Application to atrophy measurement in alzheimer's disease. In: Jiang T, Navab N, Pluim J, Viergever M (eds) Medical Image Computing and Computer-Assisted Intervention MICCAI 2010, Lecture Notes in Computer Science, vol 6362, Springer Berlin / Heidelberg, pp 610–617, DOI 10.1007/978-3-642-15745-5_75

Sommer SH, Nielsen M, Lauze FB, Pennec X (2011) A multi-scale kernel bundle for LDDMM: Towards sparse deformation description across space and scales. In: Szkely G, Hahn H (eds) Information Processing in Medical Imaging, Lecture Notes in Computer Science, vol 6801, Springer Berlin / Heidelberg, pp 624–635, DOI 10.1007/978-3-642-22092-0_51

Trouvé A (1995) An infinite dimensional group approach for physics based models in pattern recognition. Tech. rep., Johns Hopkins University

Vaillant M, Glaunès J (2005) Surface matching via currents. In: Christensen G, Sonka M (eds) Information Processing in Medical Imaging, Lecture Notes in Computer Science, vol 3565, Springer Berlin / Heidelberg, pp 1–5, DOI 10.1007/11505730_32

Vaillant M, Miller MI, Younes L, Trouvé A (2004) Statistics on diffeomorphisms via tangent space representations. NeuroImage 23, Supplement 1(0):S161–S169, DOI DOI:10.1016/j.neuroimage.2004.07.023

Younes L (2010) Shapes and diffeomorphisms. Applied Mathematical Sciences 171. Berlin: Springer., DOI 10.1007/978-3-642-12055-8

Appendix

In the following we prove Theorem 2.

Proof First we consider the variation of the kinetic energy, i.e. $\lambda_m = 0$ for all m. One directly calculates

$$(\nabla \hat{J})_t = 2\gamma \mathbf{S}\boldsymbol{\alpha}_t \ . \tag{9}$$

Let us now consider the contrary case, i.e. $\gamma = 0$. We aim to compute $\nabla_{\boldsymbol{\alpha}} E^m$ for some fixed m. Variation of $E = E^m$ w.r.t. $\boldsymbol{\alpha}_t$ in direction $\tilde{\boldsymbol{\alpha}}_t$ gives

$$\tilde{E}^m = (\partial_{\mathbf{x}_T} E)\tilde{\mathbf{x}}_T + (\partial_{\mathbf{a}_T} E)\tilde{\mathbf{a}}_T \ . \tag{10}$$

There holds

$$\tilde{\mathbf{x}}_t = \int_0^t \tilde{v}_s(\mathbf{x}_s)\, ds = \int_0^t \boldsymbol{\varphi}_s \tilde{\boldsymbol{\alpha}}_s \, ds \ . \tag{11}$$

From Theorem 1 the evolution of m-current attributes can be written as

$$\mathbf{a}_t' = \mathbf{g}(\boldsymbol{\alpha}_t, \mathbf{x}_t, \mathbf{a}_t) = \mathbf{g}_t \quad \text{with} \quad \mathbf{a}(0) = \mathbf{a}_0 \ . \tag{12}$$

Its variation in direction $\tilde{\boldsymbol{\alpha}}_t$ satisfies

$$\tilde{\mathbf{a}}_t' = (\partial_{\boldsymbol{\alpha}} \mathbf{g}_t)\tilde{\boldsymbol{\alpha}}_t + (\partial_{\mathbf{x}} \mathbf{g}_t)\tilde{\mathbf{x}}_t + (\partial_{\mathbf{a}} \mathbf{g}_t)\tilde{\mathbf{a}}_t \quad \text{with} \quad \tilde{\mathbf{a}}(0) = 0 \ .$$

It remains to express $\tilde{\mathbf{a}}_t$. We therefore introduce the flow $\frac{dF_{st}}{dt} = (\partial_{\mathbf{a}} \mathbf{g}_t) F_{st}$ with $F_{tt} = I$ and get

$$\begin{aligned}
\tilde{\mathbf{a}}_t &= \int_0^t F_{ut}((\partial_{\boldsymbol{\alpha}} \mathbf{g}_u)\tilde{\boldsymbol{\alpha}}_u + (\partial_{\mathbf{x}} \mathbf{g}_u)\tilde{\mathbf{x}}_u)\, du \\
&= \int_0^t F_{ut}(\partial_{\boldsymbol{\alpha}} \mathbf{g}_u)\tilde{\boldsymbol{\alpha}}_u \, du + \int_0^t \int_0^u F_{ut}(\partial_{\mathbf{x}} \mathbf{g}_u)\boldsymbol{\varphi}_s \tilde{\boldsymbol{\alpha}}_s \, ds \, du \\
&= \int_0^t \left(F_{ut}(\partial_{\boldsymbol{\alpha}} \mathbf{g}_u) + \int_u^t F_{st}(\partial_{\mathbf{x}} \mathbf{g}_s)\, ds\, \boldsymbol{\varphi}_u \right) \tilde{\boldsymbol{\alpha}}_u \, du \ .
\end{aligned}$$

In particular there holds

$$\tilde{\mathbf{a}}_T = \int_0^T \left(F_{tT}(\partial_{\boldsymbol{\alpha}} \mathbf{g}_t) + \int_t^T F_{sT}(\partial_{\mathbf{x}} \mathbf{g}_s)\, ds\, \boldsymbol{\varphi}_t \right) \tilde{\boldsymbol{\alpha}}_t \, dt \ . \tag{13}$$

Combining (10), (11) and (13) we have

$$\begin{aligned}
\tilde{E}^m &= \int_0^T (\partial_{\mathbf{x}_T} E)\boldsymbol{\varphi}_t \tilde{\boldsymbol{\alpha}}_t \\
&\quad + (\partial_{\mathbf{a}_T} E)\left(F_{tT}(\partial_{\boldsymbol{\alpha}}\mathbf{g}_t) + \int_t^T F_{sT}(\partial_{\mathbf{x}}\mathbf{g}_s)\,ds\,\boldsymbol{\varphi}_t\right)\tilde{\boldsymbol{\alpha}}_t\,dt \\
&= \int_0^T \Bigg(\underbrace{\left[(\partial_{\mathbf{x}_T} E) + \int_t^T (\partial_{\mathbf{a}_T} E)F_{sT}(\partial_{\mathbf{x}}\mathbf{g}_s)\,ds\right]}_{=:\boldsymbol{\eta}_t^*}\boldsymbol{\varphi}_t \\
&\quad + \underbrace{(\partial_{\mathbf{a}_T} E)F_{tT}}_{=:\boldsymbol{\zeta}_t^*}(\partial_{\boldsymbol{\alpha}}\mathbf{g}_t)\Bigg)\tilde{\boldsymbol{\alpha}}_t\,dt \\
&= \int_0^T (\boldsymbol{\eta}_t^*\boldsymbol{\varphi}_t + \boldsymbol{\zeta}_t^*(\partial_{\boldsymbol{\alpha}}\mathbf{g}_t))\tilde{\boldsymbol{\alpha}}_t\,dt\ . \qquad (14)
\end{aligned}$$

Since $F_{st}F_{ts} = I$ and $\frac{dF_{st}^*}{ds} = -(\partial_{\mathbf{a}}\mathbf{g}_s)^* F_{st}^*$ we have in particular the integral form $F_{ts}^* = I + \int_t^s (\partial_{\mathbf{a}}\mathbf{g}_u)^* F_{us}^*\,du$. This helps to simplify

$$\begin{aligned}
\boldsymbol{\zeta}_t &= F_{tT}^*(\nabla_{\mathbf{a}_T} E) = \Big(I + \int_t^T (\partial_{\mathbf{a}}\mathbf{g}_s)^* F_{sT}^*\,ds\Big)(\nabla_{\mathbf{a}_T} E) \\
&= \nabla_{\mathbf{a}_T} E + \int_t^T (\partial_{\mathbf{a}}\mathbf{g}_s)^* F_{sT}^*(\nabla_{\mathbf{a}_T} E)\,ds \\
&= \nabla_{\mathbf{a}_T} E + \int_t^T (\partial_{\mathbf{a}}\mathbf{g}_s)^* \boldsymbol{\zeta}_s\,ds \qquad (15) \\
\boldsymbol{\eta}_t &= \nabla_{\mathbf{x}_T} E + \int_t^T (\partial_{\mathbf{x}}\mathbf{g}_s)^* F_{sT}^*(\nabla_{\mathbf{a}_T} E)\,ds \\
&= \nabla_{\mathbf{x}_T} E + \int_t^T (\partial_{\mathbf{x}}\mathbf{g}_s)^* \boldsymbol{\zeta}_s\,ds\ . \qquad (16)
\end{aligned}$$

Collecting (9), (14), (15) and (16) yields the assertion. □